International Journal of Adhesion & Adhesives 19 (1999) 59–70

Analytical and experimental methods for a fracture mechanics interpretation of the microbond test including the effects friction and thermal stresses

Chun-Hsin Liu[a] and John A. Nairn[b,*]
[a] *Eastman Kodak Company, Rochester, NY 14650, USA*
[b] *Material Science and Engineering, University of Utah, Salt Lake City, Utah 84112, USA*

Accepted 17 September 1998

Abstract

An energy release rate model based on a generalized fracture mechanics of composites was developed for analyzing the microbond test. This model, which extended a previous model, includes both friction at the fiber/matrix interface and residual thermal stresses. A series of microbond tests on macroscopic specimens were carried out for evaluating the model. In some specimens we could observe debond crack growth. These results could be interpreted with a fracture mechanics R-curve which led to a measured interfacial fracture toughness. In many specimens, debond crack growth could not be observed. We developed an approximate method for determining interfacial fracture toughness even without knowledge of debond crack size. The macroscopic specimens were designed for studying the optimal approach to analysis of microbond specimens. The geometry of the macroscopic specimens, however, could also be used to measure the mode II toughness of adhesive bonds.

Keywords: B. Composites; C. Fracture Mechanics; C. Stress Analysis; D. Mechanical Properties of Adhesives; Microbond Test

1. Introduction

The microbond test is a potential method for studying fiber/matrix interfacial adhesion in composite materials.[1, 2] In a microbond test, a single cured matrix droplet is sheared from a fiber, and the stress to cause fiber/matrix interfacial debonding is measured. The measured stress must then subsequently be interpreted in terms of interfacial properties; this interpretation should be able to account for specimen geometry, residual thermal stresses, and interfacial friction effects. The most common analysis of microbond results is a simple average shear-stress failure criterion in which the average shear stress along the entire interface is equated to the interfacial shear strength.[1–7] An exact relation between the average interfacial shear stress, $\langle\tau_{rz}\rangle$, and the applied force on the fiber, F, is

$$\langle\tau_{rz}\rangle = \frac{F}{2\pi r_f l} \tag{1}$$

where r_f is the radius of the fiber and l is the length of a microbond specimen. Equating $\langle\tau_{rz}\rangle$ to the interfacial shear strength, τ_{ic}, equation (1) predicts F to be linear in l with the slope being used to determine τ_{ic}.[1, 2]

Recently, Scheer and Nairn,[8–11] argued that a critical energy release rate criterion for predicting interfacial failure is more realistic than the average shear stress failure criterion. They considered several frictionless-interface models and found that a limiting solution for long droplet lengths was sufficiently accurate for all experimental droplet lengths. Their frictionless-interface analysis lead to a simple analytical expression for energy release rate for debond growth that is independent of debond length:

$$G = \frac{r_f}{2}\left[C_{33s}\sigma_d^2 + 2D_{3s}\sigma_d\Delta T + \left(\frac{D_3^2}{C_{33}} + \frac{v_m(\alpha_T-\alpha_m)^2}{v_f A_0}\right)\Delta T^2\right] \tag{2}$$

*Corresponding author. Tel: 801 581 3413; fax: 801 581 4816
E-mail: John.Nairn@m.cc.utah.edu.

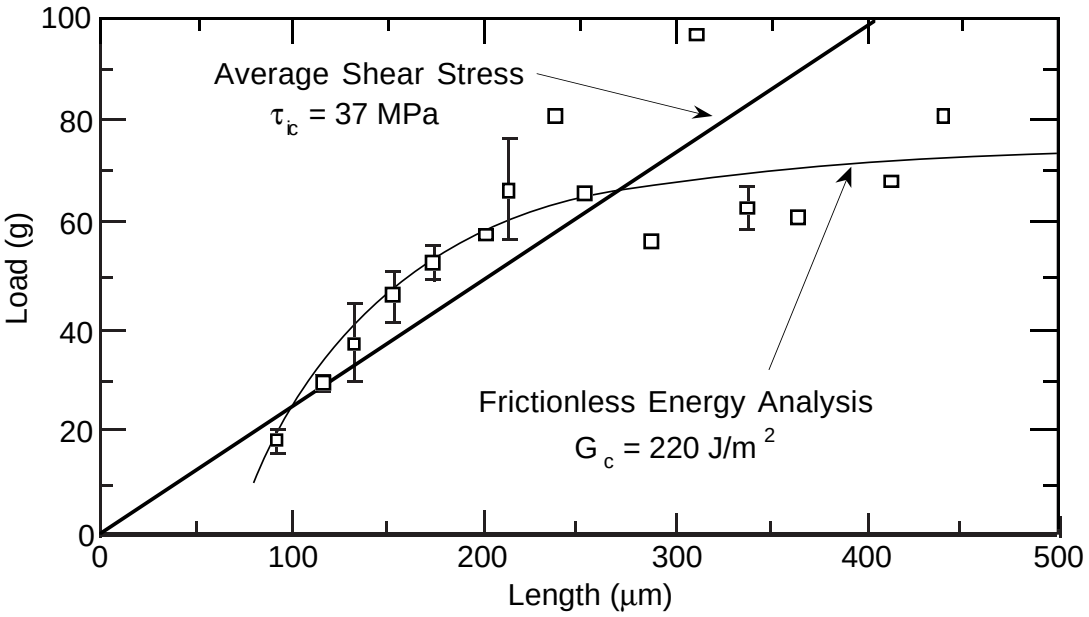

Fig. 1. Debond force as a function of droplet length for a series of Epon 828 droplets on 21 μm diameter E-Glass fibers. The smooth lines are fits to the experimental results using the average shear stress failure criterion (equation (1)) with $\tau_{ic} = 37$ MPa or using the frictionless energy model (equation (2)) with $G_{ic} = 220$ J/m^2. The experimental results are from Ref. 11.

where, $\sigma_d = F/(\pi r_f^2)$ is the stress applied to the fiber, ΔT is the temperature difference between the test temperature and the stress-free temperature, v_f and v_m are fiber and matrix volume fractions within the droplet, α_T is the transverse thermal expansion coefficient of the fiber, α_m is thermal expansion coefficient of the matrix, and C_{33s}, D_{3s}, D_3, C_{33}, and A_0 are constants, defined in the *Appendix*, which depend only on fiber and matrix properties and on specimen geometry.[9, 11] The critical energy release rate model assumes the droplet debonds when $G = G_{ic}$, where G_{ic} is an interfacial toughness. Note that equation (2) includes an extra term in the ΔT^2 term that is not given in Ref. 11. The result in equation (2) is the correct frictionless result for long droplets; the correction to Ref. 11 will be discussed further below.

Figure 1 shows some previous results for debonding of epoxy droplets from 21-μm-diameter E-Glass fibers as a function of droplet length. The smooth lines in *Figure 1* are predictions using the average shear stress model (equation (1)) or the frictionless energy release rate model (equation (2)). The energy analysis fits the experiments much better than the average shear stress analysis. The data, however, are highly scattered; the results in *Figure 1* were smoothed by taking running averages. Although we claim the experiments support the benefits of an energy analysis over an average shear stress analysis, the experiments do not represent experimental verification of the energy approach derived in Refs. 8–11.

To better clarify the energy or fracture mechanics analysis of the microbond test, we conducted a series of experiments on macroscopic microbond tests using large cylinders of epoxy of various lengths molded onto steel rods. By using macroscopic droplets we expected to reduce the scatter inherent in microscopic specimens.[2] Furthermore, by molding cylindrical droplets we could control the volume fraction of the fiber within the matrix independent of the droplet length and could better match the geometry assumptions used in the energy analysis.[8–11]

Examination of equation (2) (and the constants in the *Appendix*) reveals that G is independent of droplet length if the fiber volume fraction is held constant. In microscopic microbond tests, v_f changes with droplet length due to the natural shapes of droplets. This change in v_f plays a major role in the variation in debond force with droplet length.[10, 11] In macroscopic specimens, however, we can mold constant-radius droplets and keep v_f constant. The prediction of equation (2) is then that the debond force will be independent of droplet length. Our first experiments showed that the debond force for such specimens is not constant, but rather increases with droplet length. We concluded that the frictionless energy analysis is incomplete.

Table 1
Material properties of the steel rod and epoxy materials. The properties for the stainless steel rods are typical stainless steel properties which we did not remeasure. The tensile modulus of Epon 828 was measured; its Poisson ratio was estimated.

Property	Steel Rod	Epon 828 Epoxy
Modulus (E_A, E_T, or E_m) (GPa)	100	2.6
Shear Modulus (G_A or G_m) (GPa)	37.6	0.97
Poisson's Ratio (ν_A, ν_T, or v_m)	0.33	0.34
Thermal Expansion (α_A, α_T, or α_m) $10^{-6\circ}C^{-1}$)	14	40

Instead of abandoning fracture mechanics methods, however, we modified the energy analysis to account for friction along the interface.

This paper describes a new energy analysis that extends and corrects the results in Ref. 11; the new analysis includes both friction and residual thermal stresses. We derived an analytical expression for energy release rate for debond growth. This new result, $G(a)$, depends on debond length when friction is present, but reduces to equation (2) when friction is ignored. We used the new friction analysis to interpret experiments on macroscopic specimens for which we were able to observe crack growth along the interface. We found that all results as a function of debond length could be interpreted using fracture mechanics, provided the energy release rate calculation included both friction and residual stresses. If either effect was ignored, the results were poor. In microscopic specimens it is very difficult to observe interfacial crack growth. We thus also explored interpretation of macroscopic specimens without knowledge of interfacial crack length. We suggest the interfacial toughness can be estimated by assuming the peak debonding force corresponds to a debond length that is approximately equal to the droplet length. In other words, it is assumed that the debond propagates stably along the interface with increasing force and that a drop in force only occurs when the debond reaches the end of the droplet. Finally, besides helping understand analysis of microscopic specimen, the macroscopic specimen geometry itself is a possible method for measuring the mode II fracture toughness of adhesive bonds.

2. Materials and methods

All experiments described in this paper were done using macroscopic specimens consisting of steel rods embedded in an epoxy matrix. There are several advantages to using macroscopic specimens as model specimens. First, a large specimen size reduces the scatter inherent in microscopic specimens.[2] Second, in contrast to microscopic specimens, one has control over the shape of the macroscopic matrix. Micro-droplets naturally assume an elliptical shape. The diameter of the droplet, and hence the effective volume fraction of the fiber within the droplet (defined as volume of embedded fiber divided by total volume of embedded fiber and droplet) changes as the droplet length changes. Experimental observations show that fiber volume fraction decreases at longer droplet lengths.[11] In our macroscopic specimens, we molded cylinders of matrix onto the steel rods. By keeping the radius of the matrix cylinder constant for a series of specimens, we could keep the fiber volume fraction constant while varying the droplet length. Third, we were able to observe debond growth along the interface in some specimens. These observations allowed us to get more information from macroscopic specimens than possible from most microscopic specimens.

Stainless steel rods with diameters of 3.175 mm (0.125 in) were obtained in 3 m (10 ft) sections. The surfaces of the as-received rods were not clean. The rods where therefore cut into 125-mm-long sections, washed with detergent and distilled water, dried in air, and kept in covered containers prior to use. The material properties for the steel rods are listed in *Table 1*. The embedding epoxy matrix was Epon 828. Epon 828 consisted of a diglycidylether of bisphenol A (DGEBA) purchased from Shell Chemical Company that was cured with 14 phr of an amine curing agent, meta-phenylene diamine (m-PDA), that was purchased from the Aldrich Chemical Company. The material properties for cured Epon 828 are listed in *Table 1*.

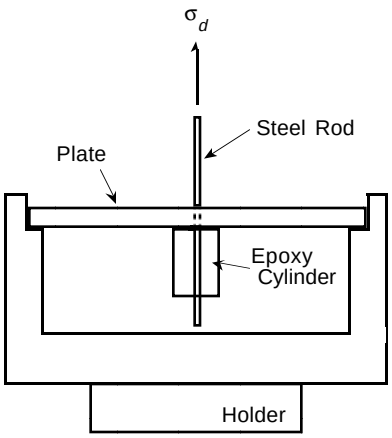

Fig. 2. A cross-section of the testing jig used for microbond tests on macroscopic specimens. The steel rod is thread through a hole in the plate and the plate is secured to the lower jig which is mounted on the testing frame. The testing-frame cross head pulls up on the end of the steel rod until the entire cylinder debonds.

The macroscopic specimens were prepared by suspending the steel rods through the center of a cylindrical mold and filling the mold with epoxy resin. The epoxy system was cured at 75°C for 2 hours and then post-cured at 125°C for 3 hours. A series of specimens with various lengths but constant fiber volume fracture were prepared. The three specimen types all had steel rod radii of 3.175 mm (0.125 in) but had outer matrix radii of 14.73 mm (0.58 in), 25.4 mm (1.0 in), and 28.58 mm (1.125 in). These three specimen types corresponded to fiber volume fractions of 4.64%, 1.56%, and 1.23%, respectively. These specimen dimensions were chosen to give fiber volume fractions in the range of 1-4% which is similar to the effective fiber volume fractions found in microscopic microbond specimens.[11] In this paper, the three specimen classes are denoted as 0.125/0.58, 0.125/1.0, and 0.125/1.125, where the first number indicates the fiber radius (in inches) and the second number indicates the matrix radius (in inches).

Figure 2 shows the testing jig for microbond tests on macroscopic specimens. The steel rod was threaded through a hole in a steel plate with a diameter slightly larger than the rod diameter. The plate was mounted to the jig in *Figure 2*, which was secured to the base of a 25 kN MTS 880 servohydraulic testing frame. Finally, the rod was pulled while force *vs.* displacement was recorded and the specimen was observed for indications of interfacial crack growth. All experiments were done at a constant displacement rate of 0.01 mm/sec. A typical force-displacement plot is shown in *Figure 3*. The force always increased linearly at first but showed some curvature before the peak. After the peak, the force dropped to a constant value which was caused by friction as the debonded droplet slid along the steel rod.

We attempted to observe interfacial crack growth during all experiments. The dark color of the epoxy prevented observation of crack growth in the larger specimens, but we were able to observe crack growth in the 0.125/0.58 specimens. In these specimens, the debond growth could be observed by eye with back-lighting. We therefore modified the testing procedure for the 0.125/0.58 specimens. Instead of loading to complete debonding, we loaded the 0.125/0.58 specimens until a small amount of debond growth was observed. We then measured the debond size and removed the loaded. This same specimen was then reloaded until some more debond growth occurred. Finally, we were able to run numerous experiments on a single specimen and record the force required to extend the debond as a function of the debond length. Similar sets of experiments were done on 0.125/0.58 specimens with lengths of 14.6 mm (0.575 in.), 29.5 mm (1.159 in.), and 44 mm (1.734 in.).

3. Fracture mechanics analysis

A previous analysis of the microbond test (see equation (2)) began with an approximate thermoelastic stress state and derived a result for energy release rate that included residual stresses but ignored friction.[8–11] Here we describe an alternative approach based on some new general fracture mechanics results for composites with residual thermal stresses.[12] In brief, we began with an exact energy release rate equation, introduced a

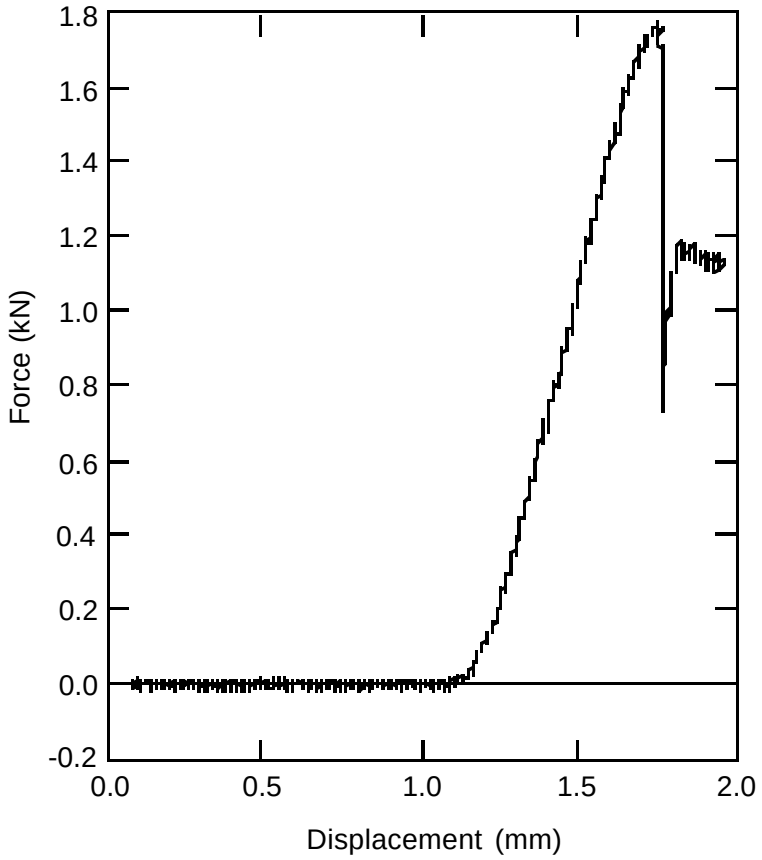

Fig. 3. A Typical force-displacement plot. This result was from a steel rod/epoxy specimen. The rod was 3.175 mm (0.125 in) in diameter, the matrix cylinder was 14.73 mm (0.58 in) in diameter and 27.97 mm (1.101 in) long.

few assumptions, and derived a thermoelastic energy release rate that depends only on the axial stress in the fiber. We then substituted a shear-lag analysis for fiber stress to derive an analytical expression for energy release rate including both residual stresses and friction. The energy release rate was found to depend on debond length. We used this energy release rate result to directly interpret crack growth experiments, like those on the 0.125/0.58 specimens, that recorded debond growth force as a function of debond length. We also suggest an approximate method for using this energy release rate result to interpret results where the debond length cannot be observed.

3.1. Energy Release Rate for Debonding

Reference 12 gives a general result for fracture analysis of composites containing residual stresses. That result assumes linear thermoelasticity and rigorously accounts for all effects of residual stresses on fracture. During crack growth, residual stresses contribute to energy release rate both by releasing thermal strain energy and by causing external work due to changes in residual displacements on the traction-loaded surfaces.[12] For traction-only loading conditions, the exact, thermoelastic energy release rate for an n-phase composite derived in Ref. 12 can be written as

$$G = \frac{d}{dA}\left(\frac{1}{2}\int_S \vec{T}^{\,0}\cdot\vec{u}\;dS\right) + \frac{V\Delta T}{2}\sum_{i=1}^{n} v_i\boldsymbol{\alpha}^{(i)}\cdot\frac{d\overline{\boldsymbol{\sigma}^{(i)}}}{dA} \tag{3}$$

where $\vec{T}^{\,0}$ and $\vec{u}$ are the surface tractions and displacements (both mechanical and thermal displacements), ΔT is the difference between the specimen temperature and the stress-free temperature, V is the total

volume, v_i is the volume fraction of phase i, $\boldsymbol{\alpha}^{(i)}$ is the thermal expansion tensor of phase i, and

$$\overline{\boldsymbol{\sigma}^{(i)}} = \frac{1}{V v_i}\int_{V_i} \boldsymbol{\sigma}^i dV \tag{4}$$

is the phase-averaged stress in phase i, where V_i indicates integration over the volume occupied by phase i. Energy release rate is found by differentiation of the key terms with respect to total fracture area A. An identical result for traction-only loading was also derived by Hashin.[13]

Figure 4 shows an idealized version of a microbond specimen. The droplet and fiber are considered as two concentric cylinders. All applied loads are assumed to be traction loads applied uniformly over the top surfaces of the fiber or matrix. If the total stress applied to the fiber (and recorded by the testing system) is σ_d, then there is a balancing stress of $-v_f\sigma_d/v_m$ applied to the top surface of the droplet. It is assumed that the bottom and side surfaces are all stress free. Applying equation (3) to the idealized specimen and allowing for an interfacial friction stress of $\tau_{rz}(r_f, z)$ on the debond surfaces, the exact energy release rate can be written as

$$\begin{aligned} G(a) &= \frac{r_f\sigma_d}{4}\frac{d}{da}\big(\langle w_f(a)\rangle - \langle w_m(a)\rangle\big) + \frac{1}{2}\frac{d}{da}\int_0^a \tau_{rz}(r_f,z)\big(w_f(r_f,z) - w_m(r_f,z)\big)dz \\ &\quad + \frac{l r_f \Delta T}{4}\left[(\alpha_A - \alpha_m)\frac{d\overline{\sigma_{zz}^{(f)}}}{da} + \alpha_T\frac{d}{da}\left(\overline{\sigma_{rr}^{(f)}} + \overline{\sigma_{\theta\theta}^{(f)}}\right) + \frac{v_m}{v_f}\alpha_m\frac{d}{da}\left(\overline{\sigma_{rr}^{(m)}} + \overline{\sigma_{\theta\theta}^{(m)}}\right)\right] \end{aligned} \tag{5}$$

Here the z-axis origin has been placed at the tip of the debond (see *Figure 4*). The first term in equation (5) is the external work on the ends of the specimen, which is a function of the difference between the average axial displacements on the fiber end, $\langle w_f(a)\rangle$, and on the matrix end, $\langle w_m(a)\rangle$. The second term accounts for friction in the form of an interfacial shear stress multiplied by the axial displacement difference at the interface, $w_f(r_f, z) - w_m(r_f, z)$. The final term arises from the second term in equation (3); it accounts for residual stress effects other than those already included in the residual stress contributions to axial displacements in the first two terms. Note that the fiber has been assumed to be transversely isotropic, with α_A and α_T being the axial and transverse thermal expansion coefficients. The matrix has been assumed to be isotropic with thermal expansion coefficient α_m. Finally, the term involving axial stress in the matrix was eliminated using force balance.

Although equation (5) is exact for concentric cylinders with uniform end traction, it contains some terms that cannot be determined analytically. Hence we introduced some assumptions. First, we divided the stress analysis into the debonded zone ($0 < z < a$) and the intact, or bonded, zone ($-(l-a) < z < 0$) (see *Figure 4*). In the debonded zone we assumed that the interfacial, friction shear stress is constant ($\tau_{rz}(r_f, z) = \text{constant}$) and that the transverse stresses are negligible ($\sigma_{rr}^{(f)} = \sigma_{\theta\theta}^{(f)} = \sigma_{rr}^{(m)} = \sigma_{\theta\theta}^{(m)} = 0$). By an exact equilibrium analysis,[15, 16] the average normal stresses in the fiber and matrix are then linear in z due to stress transfer at the interface through friction. The debonded zone *average* axial stresses thus have the form

$$\left\langle \sigma_{zz}^{(f)}(z)\right\rangle = \sigma_d + k(z-a) \qquad \text{and} \qquad \left\langle \sigma_{zz}^{(m)}(z)\right\rangle = -\frac{v_f\left\langle \sigma_{zz}^{(f)}(z)\right\rangle}{v_m} \qquad \text{for } 0 < z < a \tag{6}$$

where angle brackets ($\langle\cdot\rangle$) denote averaging over the cross section of the fiber or matrix and k is the frictional stress transfer rate defined by

$$k = \frac{2\tau_f}{r_f} \tag{7}$$

where τ_f is the absolute value of the constant interfacial friction stress. With the assumed zero transverse stresses, the average axial strains in the debonded zone, including thermal strains, are

$$\left.\begin{aligned} \left\langle \varepsilon_{zz}^{(f)}(z)\right\rangle &= \frac{\sigma_d + k(z-a)}{E_A} + \alpha_A\Delta T \\ \left\langle \varepsilon_{zz}^{(m)}(z)\right\rangle &= -\frac{v_f\big(\sigma_d + k(z-a)\big)}{E_m v_m} + \alpha_m\Delta T \end{aligned}\right\} \qquad \text{for } 0 < z < a \tag{8}$$

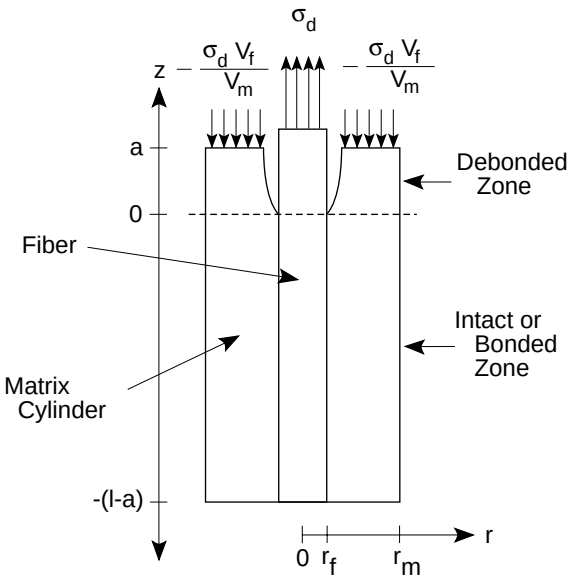

Fig. 4. The coordinate system used for the axisymmetric stress analysis of two concentric cylinders. The origin of the z axis is placed at the debond tip. The zone $0 < z < a$ is the debonded zone. The zone $-(l-a) < z < 0$ is the intact or bonded zone.

where E_A is the axial modulus of the fiber and E_m is the modulus of the matrix. Using the above stresses and strains in the debonded zone, the first term in equation (5) can be approximately evaluated. The required average end displacements are found by integrating the average axial strains:

$$\langle w_f(a)\rangle = \int_0^a \left\langle \varepsilon_{zz}^{(f)}(z)\right\rangle dz \qquad \text{and} \qquad \langle w_m(a)\rangle = \int_0^a \left\langle \varepsilon_{zz}^{(m)}(z)\right\rangle dz \tag{9}$$

The interfacial displacement discontinuity is more difficult to find because the above stress state only gives the *average* stresses. We therefore introduced another approximation that the *interfacial* displacement discontinuity is approximately equal to the difference in *average* displacements, or that

$$w_f(r_f,z) - w_m(r_f,z) \approx \langle w_f(z)\rangle - \langle w_m(z)\rangle = \int_0^z \left(\left\langle \varepsilon_{zz}^{(f)}(z)\right\rangle - \left\langle \varepsilon_{zz}^{(m)}(z)\right\rangle\right) dz \tag{10}$$

Substituting all debonded zone approximations into the first two terms in equation (5) and doing the integrations and differentiations (with verification using Mathematica[14]) gives

$$\begin{aligned}\frac{r_f\sigma_d}{4}\frac{d}{da}\big(\langle w_f(a)\rangle - \langle w_m(a)\rangle\big) + \frac{1}{2}\frac{d}{da}\int_0^a \tau_{rz}(r_f,z)\,[w_f(r_f,z) - w_m(r_f,z)]\,dz \\ \approx \frac{r_f}{2}(\sigma_d - ka)\big(C_{33s}(\sigma_d - ka) + D_{3s}\Delta T\big)\end{aligned} \tag{11}$$

where C_{33s} and D_{3s} are two terms that depend only on the fiber and matrix properties (see the *Appendix*).

For the remaining terms in equation (5) we needed to evaluate the phase-averaged normal stresses which additionally depend on the stresses in the intact or bonded zone ($-(l-a) < z < 0$). In the bonded zone, we rewrite the normal stresses as

$$\begin{aligned}\sigma_{zz}^{(f)}(r,z) &= \psi_\infty + \sigma_{zz,p}^{(f)}(r,z)\\ \sigma_{rr}^{(f)}(r,z) &= \sigma_\infty + \sigma_{rr,p}^{(f)}(r,z)\\ \sigma_{\theta\theta}^{(f)}(r,z) &= \sigma_\infty + \sigma_{\theta\theta,p}^{(f)}(r,z)\end{aligned} \qquad \text{and} \qquad \begin{aligned}\sigma_{zz}^{(m)}(r,z) &= -\frac{v_f\psi_\infty}{v_m} + \sigma_{zz,p}^{(m)}(r,z)\\ \sigma_{rr}^{(m)}(r,z) &= -\frac{v_f\sigma_\infty}{v_m}\left(1 - \frac{r_f^2}{v_f r^2}\right) + \sigma_{rr,p}^{(m)}(r,z)\\ \sigma_{\theta\theta}^{(m)}(r,z) &= -\frac{v_f\sigma_\infty}{v_m}\left(1 + \frac{r_f^2}{v_f r^2}\right) + \sigma_{rr,p}^{(m)}(r,z)\end{aligned} \tag{12}$$

Here the first term in each stress is the far-field stress, or the stress far away from any end or debond tip in infinitely long concentric cylinders. For the microbond specimen with balanced applied loads on the fiber and matrix, the net axial load is zero. Thus, the far-field stresses are purely the residual stresses in two infinitely long cylinders with different thermal expansion coefficients. Analytical results for the far-field axial fiber stress and interfacial radial stress are

$$\psi_\infty = -\frac{D_3\Delta T}{C_{33}} \qquad \text{and} \qquad \sigma_\infty = \frac{v_m}{v_f A_0}\left(\frac{A_3 D_3}{C_{33}} - (\alpha_T - \alpha_m)\right)\Delta T \tag{13}$$

where the constants A_0, D_3, and C_{33} depend only on fiber and matrix properties and are defined in the *Appendix*.[11] The second term in each stress is the perturbation stress, or the change in stress caused by the debond tip or the specimen ends. In this approximate analysis, we assumed the transverse perturbation stresses are negligible ($\sigma^{(f)}_{rr,p}(r,z) = \sigma^{(f)}_{\theta\theta,p}(r,z) = \sigma^{(m)}_{rr,p}(r,z) = \sigma^{(m)}_{rr,p}(r,z) = 0$). The *average* axial and transverse stresses can then be written as

$$\left.\begin{aligned}
\left\langle \sigma^{(f)}_{zz}(z)\right\rangle &= \psi_\infty\big(1 - F(z-a+l)\big) + (\sigma_d - k\,a - \psi_\infty)F(-z)\\
\left\langle \sigma^{(f)}_{rr}(z) + \sigma^{(f)}_{\theta\theta}(z)\right\rangle &= 2\sigma_\infty\\
\left\langle \sigma^{(m)}_{zz}(z)\right\rangle &= -\frac{v_f\left\langle \sigma^{(f)}_{zz}(z)\right\rangle}{v_m}\\
\left\langle \sigma^{(m)}_{rr}(z) + \sigma^{(m)}_{\theta\theta}(z)\right\rangle &= -\frac{2v_f\sigma_\infty}{v_m}
\end{aligned}\right\} \text{ for } -(l-a) < z < 0 \tag{14}$$

where $F(z)$ is a solution for the average fiber stress in two concentric cylinders having axial fiber stress equal to 1 and a balancing matrix axial stress of $-v_f/v_m$ at $z = 0$ and all stresses 0 at $z = l - a$. The required phase-averaged stresses in terms of average stresses can be evaluated using

$$\overline{\sigma^{(m \text{ or } f)}_{ij}} = \frac{1}{l}\int_{-(l-a)}^{a}\left\langle \sigma^{(m \text{ or } f)}_{ij}\right\rangle dz \tag{15}$$

Evaluating all phase-averaged stresses (including contributions from both the bonded and debonded zones), differentiation, and substitution into equation (5) together with the result in equation (11) results in

$$\begin{aligned}
G(a) &= \frac{r_f}{2}C_{33s}(\sigma_d - ka)^2 + \frac{r_f}{2}D_{3s}\big(2 + C'_T(a)\big)(\sigma_d - ka)\Delta T\\
&\quad + \frac{r_f}{2}\left[\left(\frac{D_3^2}{C_{33}} + \frac{v_m(\alpha_T - \alpha_m)^2}{v_f A_0} + \frac{2D_3 D_{3s}}{C_{33}}C'_T(a)\right)\Delta T^2 - kD_{3s}C_T(a)\Delta T\right]
\end{aligned} \tag{16}$$

where $C_T(a)$ is a cumulative stress transfer function defined by integrating $F(z)$ or

$$C_T(a) = \int_0^{l-a} F(z)\,dz \tag{17}$$

In the absence of friction ($k \to 0$) and in the limit of long droplets ($C'_T(a) \to 0$) this new result reduces exactly to equation (2), or the previous frictionless, long-droplet-limit result. In other words, equation (16) extends the previous fracture mechanics analysis of the microbond specimen to account for friction at the interface. In the frictionless limit, there is one difference between this new result and the previous model in Refs. 8–11. This new result (see equation (2)) includes an extra term in the ΔT^2 term of $v_m(\alpha_T - \alpha_m)^2/(v_f A_0)$. An examination of the calculations in Refs. 8–11 revealed a minor error in the energy calculations that neglected this term. The results quoted in equations (2) and (16) correct this error.

One final term remains before equation (16) can give an explicit result for energy release rate, namely the cumulative stress transfer function, $C_T(a)$. We emphasize that equation (16) only makes a few assumptions, all of which are expected to be accurate. Thus equation (16) should be accurate provided a sufficiently accurate $C_T(a)$ is used. Here we evaluated $C_T(a)$ using a simple shear-lag model. We limited our analysis to a shear-lag model because comparison to numerical results discussed below indicate the shear-lag solution is sufficiently accurate. There remains, however, a potential for improved results simply by using improved

results for $C_T(a)$. One could, in principle, even experimentally determine $C_T(a)$ by integration of fiber stresses extracted from Raman experiments on microbond specimens.[17] The point is that equation (16) reduces the debonding energy release rate to the problem of determining stress transfer into the fiber. Future models can focus on the stress transfer problem rather than the energetics of debonding.

A simple shear-lag analysis (see Ref. 15 for a recent discussion of the proper approach to shear-lag analysis of fiber/matrix specimens) for two concentric cylinders with the boundary conditions discussed above for $F(z)$ quickly leads to

$$F(z) = \frac{\sinh \beta(l-a-z)}{\sinh \beta(l-a)} \tag{18}$$

where β is the shear-lag parameter defined by[15, 16, 18]

$$\beta^2 = \frac{2}{r_f^2 E_A E_m} \left[\frac{E_A v_f + E_m v_m}{\frac{v_m}{4G_A} + \frac{1}{2G_m}\left(\frac{1}{v_m}\ln\frac{1}{v_f} - 1 - \frac{v_f}{2}\right)} \right] \tag{19}$$

Note that this shear-lag parameter is different than the Cox parameter[19] commonly quoted in the literature. The Cox parameter is incorrect while the parameter in equation (19), originally derived by Nayfeh,[18] has been shown to give correct results for finite specimens such as microbond specimens.[15] Integration of $F(z)$ leads to

$$C_T(a) = \frac{1}{\beta}\left[\coth \beta(l-a) - \operatorname{csch} \beta(l-a)\right] \tag{20}$$

$$C_T'(a) = -\frac{1}{2}\operatorname{sech}^2\left(\frac{\beta(l-a)}{2}\right) \tag{21}$$

3.2. Comparison to Finite Element Analysis

The accuracy of the analytical model was verified by comparison to finite element calculations (FEA). In brief, macroscopic specimens were analyzed using axisymmetric, 8-noded, isoparametric elements. The energy release rate as a function of debond length was found by a modified crack closure technique.[20] For a wide range of specimen geometries and loading conditions (one of which in shown in *Figure 5*) we always found excellent agreement between the analytical result in equation (16) and the numerical FEA results provided the debond tip was in the central portion of the specimen. The analytical results and FEA results did not agree when the debond tip was too close to either specimen end. The analytical result probably does not correctly account for end effects; for example, the negative analytical results when $a \approx l$ are nonphysical. We further note that the FEA results were very difficult when the debond tip was near either end. We suggest that neither the analytical result nor the FEA result give accurate results near the ends, but that both give accurate results away from the ends. More details on the comparison to FEA results are given in Ref. 21.

The analytical model gives total energy release rate. In other words, the analytical model does not partition the energy release rate into mode I and mode II energy release rates. The FEA calculations, however, show that except for very short debond lengths (where accuracy is questionable), the debond crack growth is nearly pure mode II fracture. We thus expect the microbond test to be producing predominantly mode II fracture. Any toughness determined from microbond tests will be a mode II interfacial fracture toughness.

4. Results and discussion

4.1. Specimens With Observed Debond Growth

In all 0.125/0.58 specimens, we were able to observe stable debond growth. By doing repeated loading experiments with different initial debond lengths, we recorded the stress to cause debond growth, σ_d, as a function of debond length, a. By coupling these experiments with equation (16) we can construct a crack resistance or R-curve for interfacial fracture by plotting $G(a)$ as a function of a; a $G(a)$ calculated from

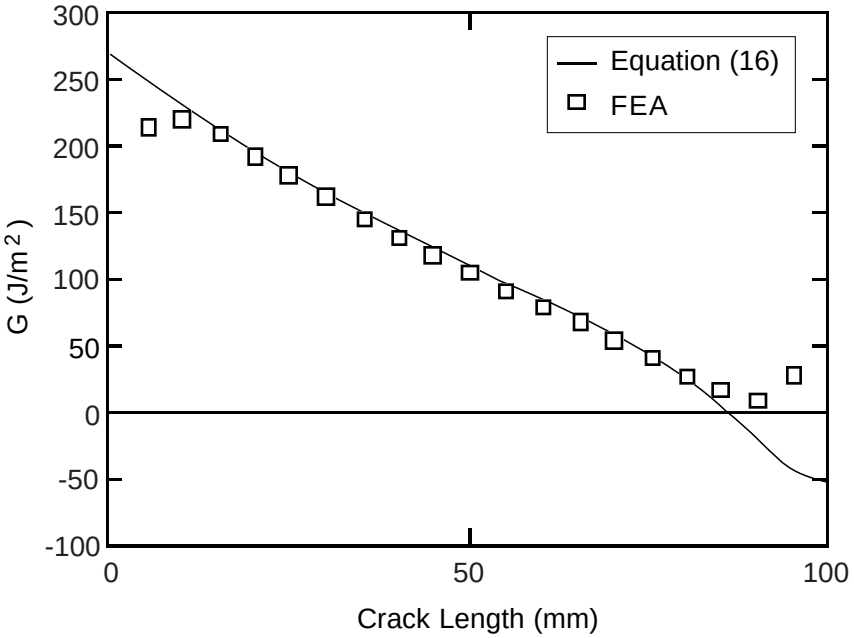

Fig. 5. A comparison of the energy release rate calculated by equation (16) (smooth line) and by finite element analysis (symbols). This sample calculation was for a 0.125 in diameter steel rod embedded in a 1.25 in diameter matrix cylinder of length 100 mm. The fiber volume fraction was 1%. The loading conditions were $\sigma_d = 100$ MPa, $\tau_f = 1$ MPa, and $\Delta T = -95°$C.

experimental crack growth is a *critical* energy release rate or interfacial fracture toughness denoted here by G_{ic}. If our fracture mechanics analysis is a valid analysis for these specimens, the R-curve should be flat or $G(a)$ should be independent of a and equal to G_{ic}. Alternatively, as observed in many materials, the R-curve might have an initial rapid rise followed by a flat plateau.[22] For such materials the plateau value is equated to the toughness, G_{ic}.

Figure 6 gives the results of analyzing experiments on a single 0.125/0.58 specimen four different ways. The specimen considered had a length of 44 mm; the fiber volume fraction was 4.64%. To use equation (16), we needed to input the thermomechanical properties of the fiber and matrix, the magnitude of the interfacial friction (τ_f), and the level of residual thermal stresses (ΔT). The assumed thermomechanical properties are given in *Table 1*. The different curves in *Figure 6* correspond to different assumptions about τ_f and ΔT.

Curve a in *Figure 6* is an analysis that ignores both residual stresses and interfacial friction. This curve is clearly a poor fracture mechanics result; it is never constant. Furthermore, the absolute values of $G_{ic}(a)$, ranging as high as 1200 J/m^2, are probably unrealistically high for a steel/epoxy interface. Curve b includes residual thermal stresses, but ignores friction. This analysis is identical to the simple, frictionless energy analysis described in Ref. 11 and equation (2). The residual thermal stresses were included by setting $\Delta T = -95°$C, which is close to the temperature difference between the post-cure temperature (125°C) and the testing temperature (room temperature). Curve b, like curve a, is a poor fracture mechanics result. It is simply shifted to higher G_{ic} values than curve a; the magnitude of the shift corresponds to the energy released by the residual stresses.

Curves c and d (filled symbols in *Figure 6*) both include friction effects, but to include friction we needed to input a value for τ_f. Our approach was to assume that the interfacial friction stress during debond growth is equal to the interfacial friction after complete debonding. This later interfacial friction can be measured from the force-displacement curve by dividing the sliding force after debonding by the total embedded fiber area ($2\pi r_f l$). Some alternative friction assumptions are discussed below. For the 0.125/0.58 specimens, the post-debonded friction stress was 4.2 MPa. Curve c is an analysis that included both residual stresses and friction. This curve is a good fracture mechanics result. There is evidence for an initial rise in G_{ic} at short debond lengths, but the R-curve soon levels out at an approximately constant value of about $G_{ic} = 360$ J/m^2. This value for G_{ic} is a reasonable toughness for a steel/epoxy interface.

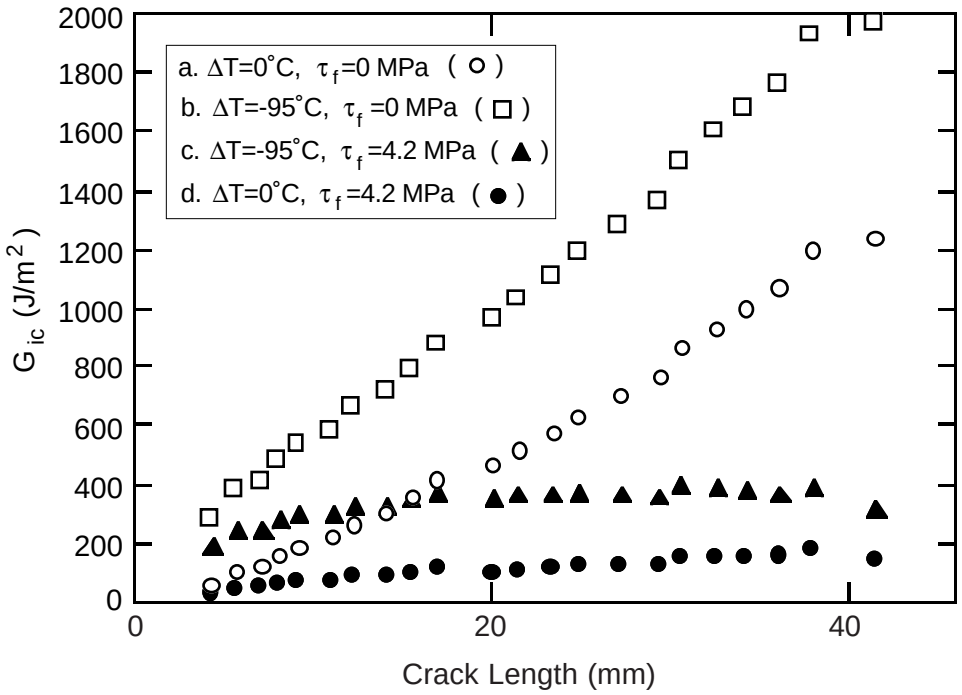

Fig. 6. Crack-resistance curves for a single 0.125/0.58 specimen analyzed four different ways. Curve *a* ignores residual stresses and friction; curve *b* includes residual stresses but ignores friction; curve *c* includes both residual stresses and friction; curve *d* ignores residual stresses, but includes friction.

Curve *c* was a good result, but we calculated a fourth result in curve *d* to assess the role of residual stresses in the fracture process. Curve *d* includes interfacial friction, but ignores residual stresses. Although curve *d* looks relatively flat on the scale of *Figure 6* it starts at a low G_{ic} and gradually increases to G_{ic} of about 200 J/m^2 without ever leveling off. The significance of curve *d* is its difference from curve *c*. That difference illustrates the magnitude of the contribution of residual stress to debonding. The magnitude is large; in fact, most of the energy released comes from residual stresses.

The stress state during debond growth is certainly much different than the stress state during post-debonding sliding. A concern arises as to whether or not the post-debond frictional stress is an acceptable input value for τ_f in the calculation of G_{ic}. Curves *b* and *c* in *Figure 6* differ only in the value used for τ_f. We could similarly create a family of *R*-curves by varying τ_f. If we accept that the *R*-curve should be as flat as possible, an alternative scheme to finding τ_f would be to vary τ_f until the R-curve is optimally flat. We tried this approach for the data in *Figure 6*; the optimal value for τ_f was indistinguishable from the τ_f value deduced from the post-debond sliding force. We thus claim that the post-debond sliding force is an appropriate and accurate method for determining the magnitude of the friction stress during debonding.

A third alternative to inclusion of interfacial friction is to model friction as a Coulomb friction process in which interfacial shear stress is proportional to interfacial radial stress

$$\tau_{rz}(r_f, z) = \mu\sigma_{rr}(r_f, z) \tag{22}$$

where μ is the coefficient of friction. Our global analysis method, however, does not accurately include $\sigma_{rr}(r_f, z)$; in other words, explicit inclusion of Coulomb friction at the micromechanics level is not possible. In a linear elastic analysis, $\sigma_{rr}(r_f, z)$ will be linearly related to boundary conditions. We could therefore empirically include Coulomb friction by setting $\tau_{rz}(r_f, z)$ proportional to σ_d. Such an analysis can be derived from our analysis by setting $\tau_f = \mu_{eff}\sigma_d$, where μ_{eff} is an *effective* coefficient of friction. Such an approach would not lead to an improved *R*-curve analysis of the our results. Within the accuracy of the experiments, it is therefore acceptable to treat τ_f as a constant that describes the *effective* or perhaps *average* interfacial friction stress throughout the debonding process. Furthermore, it is possible that interfacial shear stress in the debond zone is not entirely caused by Coulomb friction but rather by other residual interfacial adhesion

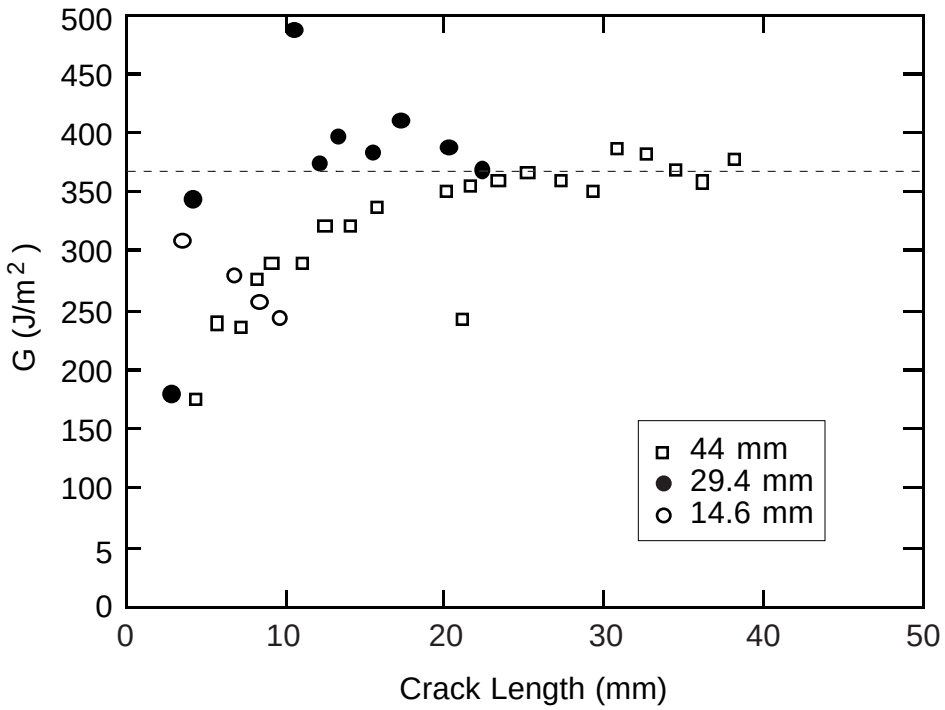

Fig. 7. Crack-resistance curves for three different 0.125/0.58 specimens with different length. The R-curves were calculated using an analysis that includes both residual stresses and interfacial friction. The dashed line is drawn at a plateau toughness of about $G_{ic} = 360$ J/m^2.

effects. An *effective* friction stress model can approximately account for such effects, while a Coulomb friction model is tied in to a specific physical mechanism for interfacial shear stress.

Figure 7 shows the calculated R-curves for three 0.125/0.58 specimens with three different lengths. If G_{ic} is a material property, the R-curves from different length samples should be the same. There was experimental scatter and only the data from the 44-mm-long specimen gave sufficient results to clearly show a flattening R-curve. The shorter specimens, by necessity, could only include data with debond lengths up to the total specimen length. We also noted that the data at the longest debond lengths (a near l) were consistently low. This error was a consequence of the calculated $G(a)$ being wrong and too low as $a \to l$ (see *Figure 5*); we therefore ignored the last point with the longest a from each specimen. Despite the limited data from the shorter specimens, we claim all results are consistent with there being a unique, fracture-mechanics R-curve for the steel/epoxy interface. Furthermore, the previously determined plateau toughness of $G_{ic} = 360$ J/m^2 is consistent with the results from the shorter specimens.

In summary, we get a reasonable fracture mechanics analysis of our macroscopic microbond specimens provided we can measure debond force as a function of debond length and provided we interpret the results using an energy release rate analysis that includes *both* residual thermal stress and interfacial friction. The thermal stresses can be estimated from the difference between the curing temperature and the testing temperature. The interfacial friction stress can be estimated from the post-debond sliding force in the force-displacement results. If either residual stresses or friction are ignored, the resulting R-curve will not be flat and a G_{ic} calculated from any particular experimental result will be wrong. Notice also, that besides providing model specimens for studying the microbond test, the concentric cylinder geometry, with the inner cylinder being a substrate and the outer cylinder being an adhesive, could be used to measure the mode II fracture toughness of adhesive bonds.

4.2. Specimens Without Observed Debond Growth

In many microbond tests, it may be difficult or impossible to observe and measure debond growth. For example, we were not able to observe debond growth in the 0.125/1.0 or 0.125/1.125 specimens, due in part to the larger amount of epoxy and to the dark color of the cured matrix. Similarly, most experiments on microscopic microbond specimens record only debonding force and are not able to observe debond growth.[1–11] In this section we propose a potential scheme for evaluating interfacial fracture toughness from microbond tests by using experiments that record only the peak debonding force as a function of total droplet length. We judged the results by how well they could reproduce the toughness measured from the debond growth specimens of $G_{ic} = 360$ J/m^2.

The analytical and numerical results in *Figure 5* show that, in the presence of friction and at a constant σ_d, the debonding energy release rate decreases as the debond grows. The consequence of this behavior is that debond growth is predicted to be stable. This prediction agrees with our observations on the 0.125/0.58 specimens. When we connected our debond growth observations to the force-displacement plot, we noted that force continued to increase as the debond grew and that the peak force corresponded to the point at which the debond reached the end of the droplet. In other words, the peak debond force, which is easily measurable, corresponds to a debond specimen with debond length, a, approximately equal to droplet length, l, which is also easily measurable.

We propose that interfacial fracture toughness in specimens without observed debond growth can be estimated by taking the debond stress, σ_d, from the peak force and evaluating the energy release rate as a approaches l:

$$G_{ic} = \lim_{a \to l} G(a) \tag{23}$$

A problem, arises, however, that when $a \approx l$ the analytical result is inaccurate and we additionally lack confidence in the FEA results. We therefore developed an approximate alternative. *Figure 8* shows some sample plots of $G(a)$ for various droplet lengths and for a limiting analysis as $l \to \infty$. At short debond lengths, $G(a)$ is independent of l. This situation corresponds to the debond tip being far away from the droplet end. As $a \to l$, $G(a)$ drops and, as discussed above, becomes inaccurate. We suggest that an acceptable $G(a = l)$ can be estimated by calculating $G(a)$ from the energy release curve for a droplet that has a much larger length than the actual droplet. In fact, we get well-behaved results simply by calculating $G(a)$ in the long-droplet limit or the limit as $l \to \infty$. The limits on the stress-transfer functions are

$$\lim_{l \to \infty} C_T(a) = \frac{1}{\beta} \qquad \text{and} \qquad \lim_{l \to \infty} C_T'(a) = 0 \tag{24}$$

The limiting energy release rate, $G_\infty(a) = \lim_{l \to \infty} G(a)$, is thus

$$G_\infty(a) = \frac{r_f}{2}\left[C_{33s}(\sigma_d - ka)^2 + D_{3s}\left(2\sigma_d - k\left(2a + \frac{1}{\beta}\right)\right)\Delta T + \left(\frac{D_3^2}{C_{33}} + \frac{v_m(\alpha_T - \alpha_m)^2}{v_f A_0}\right)\Delta T^2\right] \tag{25}$$

Figure 9 plots the calculated R-curve from the 0.125/1.0 and 0.125/1.125 specimens. G was calculated using equation (25), with a equal to the droplet length and σ_d derived from the peak force in the force-displacement plot. The dashed line through *Figure 9* is for $G_{ic} = 360$ J/m^2 that was measured from the 0.125/0.58 specimens with observed debond growth. These results form a new R-curve. There is a rising region at short droplet length, but the results level off in a plateau region that is consistent with the measured toughness of $G_{ic} = 360$ J/m^2. There is more scatter in this estimated R-curve than in the more rigorous R-curve in *Figure 7*. There also seems to be a consistent downward trend in the 0.125/1.0 specimens for longer droplet lengths. There are two possible causes for this drop. First, there may be inaccuracies in the approximate scheme of estimating $G(a = l)$ from equation (25). Perhaps this method works best for shorter droplet lengths. Second, friction becomes increasingly important for longer debonds or here for longer droplet lengths. We, unfortunately, only made limited friction observations for the specimens in *Figure 9*. From our few recorded results we estimated the friction to be 4 MPa in the 0.125/1.0 specimens and 5 MPa in the 0.125/1.125 specimens. It is possible that more accurate friction observations could both reduce the scatter and eliminate the downward trend at long droplet lengths. The preferred approach for finding G without observed debond growth is to record a specific friction result for each individual specimen.

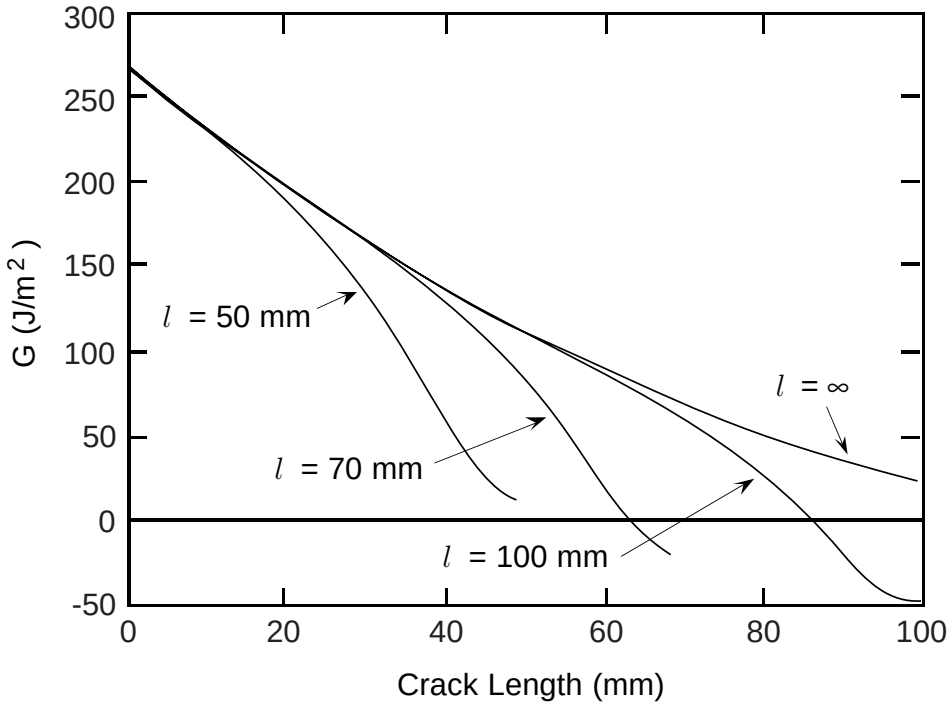

Fig. 8. Energy release rate as a function of debond length for steel/epoxy specimens calculated using the analytical model with $\sigma_d = 100$ MPa, $\tau_f = 1$ MPa, $\Delta T = -95°$C, and $v_f = 1\%$. The four curves are for three different droplet lengths and the limiting results as $l \to \infty$.

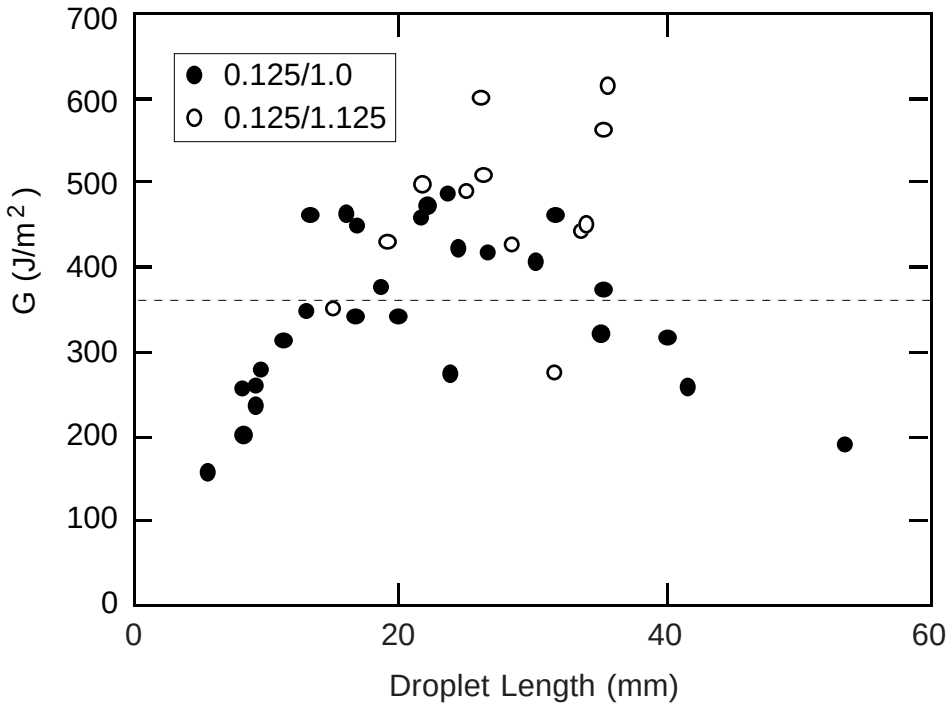

Fig. 9. An approximate R-curve for the 0.125/1.0 specimens and the 0.125/1.125 specimens. G was calculated by assuming the debond length was equal to the droplet length at the time of the peak force. $G(a = l)$ was estimated using equation (25).

The observation that $G(a) \approx G_\infty(a)$ provided $a << l$ allows us to assess the impact that our use of shear-lag analysis has on the accuracy of $G(a)$. From equation (25) we see that the only contribution of the shear-lag terms to total energy release rate is the term $1/\beta$ which arises from the limiting value for $C_T(a)$. In other words, the only result we require from shear-lag analysis is an estimation of the average axial stress in the fiber. The results in Ref. 15 show that average axial stress calculated by shear-lag analysis is reasonably accurate; it was found to always be within 10% of the correct result provided the fiber volume fraction is not too low and provided one uses the correct β (as given in equation (19)). The error in $C_T(a)$, or the *integral* of average axial fiber stress, will probably be even less than 10%. We concluded that detailed knowledge of $F(z)$ is not crucial to an accurate result for $G(a)$. As corollaries, we claim that shear-lag analysis is a sufficiently accurate tool for our energy release rate analysis and that efforts at improved stress analysis results for $F(z)$ should not have much effect on the calculated $G(a)$.

4.3. Reanalyzing Literature Results

Many experimental microbond results have been reported in the literature; most have been analyzed using the average shear stress failure criterion.[1–7] Can that data be reanalyzed using the fracture methods of this paper? The answer, unfortunately, is normally no. The fracture mechanics analysis requires experiments that measure debond force as a function of droplet length, record the droplet diameter of each specimen (to be used to calculate the *effective* fiber volume fraction in the droplet[11]), estimate friction from the post-debonding sliding stress, and reports the expected level of residual stresses. Most literature results report only the peak debond force and the total droplet length. One exception are the results in Ref. 11 which reported all required terms except for the estimated friction stress. These results are the ones plotted in *Figure 1*. We attempted reanalysis of these microscopic specimen experiments using the method proposed in the previous section for specimens without observed debond growth.

Because we did not know the friction stress, we treated the friction stress as an adjustable parameter and constructed R-curves as a function of τ_f. The result when $\tau_f = 0$ corresponds to the analysis in Ref. 11 and plotted in *Figure 1* (although not as an R-curve). This analysis gave a toughness of $G_{ic} = 220$ J/m^2. The resulting R-curve (plot not shown) was highly scattered and we could not judge whether or not it was flat. As we increased friction, the calculated G_{ic} decreased and there was no apparent improvement in the R-curve plot. For example, a friction stress of 5 MPa led to a toughness estimation of $G_{ic} = 157$ J/m^2. We concluded that it is impossible to verify the fracture mechanics approach to the microbond test by analysis of scattered experimental data on microscopic specimens. If we accept the fracture mechanics analysis, however, we find that an analysis that ignores friction gives an *upper bound* to the correct interfacial fracture toughness. The calculated toughness always drops as τ_f increases; it will become equal to the physically correct toughness only when τ_f is equal to the actual friction on the debond surfaces.

4.4. Recommended Microbond Test Procedure

Based on our experiments on macroscopic specimens, we can recommend test methods for microscopic specimens. These recommendations could also be applied to other macroscopic specimens for measuring the mode II toughness of adhesive bonds. The recommended experiments are to make a series of droplets with different length droplets and record length *and* diameter for each droplet. The diameter of the droplet can be used to estimate v_f by assuming the natural droplet shape is elliptical for microscopic specimens[11] or cylindrical for macroscopic specimen. Each specimen should then be subjected to a standard microbond test. If possible, one should observe debond growth and record the force required to extend the debond as a function of debond length. If debonds cannot be observed, then one should record peak debond force. For all experiments, the friction stress should be estimated from the post-debond sliding stress. The described set of data is sufficient to calculate an R-curve and therefore to estimate a mode II interfacial fracture toughness. If debond growth cannot be observed, the R-curve should be calculated using equation (25) with a for each specimen equated to the droplet length. If debond growth can be observed, the R-curve should be calculated using equation (16). Because equation (16) becomes inaccurate as $a \to l$, the results at large a should be ignored or they should be interpreted using the limiting result in equation (25) instead of equation (16).

Acknowledgements

This work was supported by a grant from the Mechanics of Materials program at the National Science Foundation CMS-9713356.

Appendix

The defined A_i, C_{ij}, and D_i required for the calculations described in this paper are listed below:

$$v_f A_0 = \frac{v_m(1-\nu_T)}{E_T} + \frac{v_f(1-\nu_m)}{E_m} + \frac{1+\nu_m}{E_m} \tag{26}$$

$$A_3 = -\left(\frac{\nu_A}{E_A} + \frac{v_f\nu_m}{v_m E_m}\right) \tag{27}$$

$$C_{33} = \frac{1}{2}\left(\frac{1}{E_A} + \frac{v_f}{v_m E_m}\right) - \frac{v_m A_3^2}{v_f A_0} \tag{28}$$

$$C_{33s} = \frac{1}{2}\left(\frac{1}{E_A} + \frac{v_f}{v_m E_m}\right) \tag{29}$$

$$D_3 = -\frac{v_m A_3}{v_f A_0}[\alpha_T - \alpha_m] + \frac{1}{2}[\alpha_A - \alpha_m] \tag{30}$$

$$D_{3s} = \frac{1}{2}(\alpha_A - \alpha_m) \tag{31}$$

Here v_f and v_m are the volume fractions of fiber and matrix within the droplet. For the concentric cylinders in macroscopic specimens

$$v_f = \frac{r_f^2}{r_m^2} \qquad \text{and} \qquad v_m = \frac{r_m^2 - r_f^2}{r_m^2} \tag{32}$$

E_A and E_T are the axial and transverse moduli of the fiber, ν_A and ν_T are the axial and transverse Poisson's ratios of the fiber, E_m is the modulus of the matrix, ν_m in the Poisson's ratio of the matrix, α_A and α_T are the axial and transverse thermal expansion coefficients of the fiber, and α_m is the thermal expansion coefficient of the matrix. The fiber is treated as transversely isotropic with the axial direction along the axis of the fiber. The results for isotropic fibers are easily generated be setting $E_A = E_T = E_f$, $\nu_A = \nu_T = \nu_f$, and $\alpha_A = \alpha_T = \alpha_f$ where subscript f indicates thermomechanical properties of an isotropic fiber. The matrix is here always considered to be isotropic.

References

1 Miller, B., Muri, P. and Rebenfeld, L. *Comp. Sci. & Tech.* 1987, **28**, 17–32.
2 Gaur, U. and Miller, B. *Comp. Sci &. Tech.* 1989, **34**, 35–51.
3 Haaksma, R. A. and Cehelnik, M. J. *Mat. Res. Soc. Symp. Proc.* 1990, **170**, 71–76.
4 Chou, C. T. and Penn, L. S. *J. Adhesion* 1991, **36**, 125–137.
5 Rao, V., Herrera-Franco, P., Ozzello, A. D. and Drzal, L. T. *J. Adhesion* 1991, **34**, 65–77.
6 Tesoro, G. C., Benrashid, R., Rebenfeld, L. and Gaur, U. in 'International Symp. on Polymers for Advanced Technologies', 17-21 August 1987, Jerusalem, Israel, 773–791.
7 Wagner, H. D., Gallis, H. E., and Wiesel, E. *J. Mat. Sci.* 1993, **28**, 2238–2244.
8 Scheer, R. J. and Nairn, J. A. *Composites Engineering* 1992, **2**, 641–654.
9 Nairn, J. A. and Scheer, R. J. *Third Int'l Conf. on Deformation and Fracture of Composites* 1995, 616–625.
10 Scheer, R. J. 'An Energy Based Analysis of Fiber-Matrix Adhesion', Ph.D. Thesis, University of Utah, 1993.
11 Scheer, R. J. and Nairn, J. A. *J. Adhesion* 1995, **53**, 45–68.
12 Nairn, J. A. *J. Applied Mech.* 1997, **64**, 804–810.

13 Hashin, Z. *J. Mech. Phys. Solids* 1996, **44**, 1129–1145.
14 Mathematica Version 2.2, Wolfram Research, Champaign, Illinois, 1994.
15 Nairn, J. A. *Mech. of Materials* 1997, **26**, 63–80.
16 McCartney, L. N. in 'Local Mechanics Concepts for Composite Material Systems' (Eds., J. N. Reddy and K. L Reifsnider), Proc. IUTAM Symposium, Blacksburg, VA, 1991, 251–282.
17 Andrews, M. C., Bannister, D. J. and Young, R. J. *J. Mat. Sci.* 1996, **31**, 3893–3913.
18 Nayfeh, A. H. *Fibre Sci. & Tech.* 1977, **10**, 195–209.
19 Cox, H. L. *Brit. J. Appl. Phys.* 1952, **3**, 72–79.
20 Krishnamurthy, T., Ramamurthy, T. S., Vijayakumar, K. and Dattaguru, B. in 'Proc. Int. Conf. Finite Elements in Computational Mechanics', 2-6 December 1985, Bombay, India, 891–900.
21 Liu, C.-H. 'New Energy Release Rate Models for the Microbond Test', Ph.D. Thesis, University of Utah, 1997.
22 Atkins, A. G. and Mai, Y.-W. 'Elastic and Plastic Fracture', John Wiley & Sons, New York, 1985.